Pergamon

Cement and Concrete Research 30 (2000) 1453–1464

CEMENT AND CONCRETE RESEARCH

Damage assessment in reinforced concrete using spectral and temporal nonlinear vibration techniques

Koen Van Den Abeele[a,*], Joëlle De Visscher[b]

[a]Laboratory of Building Physics, Catholic University Leuven, Celestijnenlaan 131, B-3001 Heverlee, Belgium
[b]Department of Mechanics of Materials and Constructions (MEMC), Free University Brussels, Pleinlaan 2, 1050 Brussels, Belgium

Received 7 December 1999; accepted 2 June 2000

Abstract

Both linear and nonlinear (amplitude-dependent) acoustical experiments are performed on a reinforced concrete (RC) beam in which damage is gradually induced by means of static loading tests. At different levels of damage, a complete experimental modal analysis (EMA) is carried out, assuming the structure to behave linearly. The analysis in terms of modal curvatures indicates a gradual reduction of the bending stiffness along the beam. Strong amplitude dependence of the linear dynamic behavior is observed as damage increases. After each loading step, measurement of resonant frequencies and damping ratios as function of vibration amplitude are performed, both using a frequency domain technique and a time domain technique. The nonlinearity is quantified as function of the damage. We compare the results of the linear and nonlinear techniques, and value them against visual damage and local bending stiffness.

Keywords: Crack detection; Microcracking; Durability; Fatigue; Physical properties

1. Introduction

Reinforced concrete (RC) structures are subject to microcrack initiation and propagation at load levels far below the actual failure load. While visual inspection fails to assess the damage at this early stage, vibration measurements are sufficiently sensitive to detect and monitor the damage evolution, even when the microcracks are situated in hidden or internal zones. However, most currently used vibration techniques are linear techniques, based on the loss of stiffness (or equivalently wave speed), or the increase of attenuation with damage. Generally, the sensitivity of such methods to microscale damage is not extraordinary. Recently, new techniques were developed that focus on the nonlinearity or amplitude dependence of the material's complex moduli (real and imaginary parts, i.e., wave speed and damping) [1–4]. These techniques particularly probe second-order effects on wave propagation at small strain levels, such as the generation of harmonics and intermodulated frequencies, resonant frequency shift as function of applied drive voltage, nonlinear attenuation, etc. To investigate microcracking in quasi-brittle structures such as RC, nonlinear vibration measurements prove to be superior compared to linear techniques, primarily because RC is intrinsically nonlinear and because the degree of nonlinearity is highly related to the amount of damage. The purpose of this paper is to illustrate these nonlinear acoustic methods, and to highlight the extreme sensitivity of their results to progressive microcrack damage in RC.

In Section 2, we describe the sample and the loading procedure which is used to gradually induce damage in the sample. In Section 3, we summarize the results of a linear modal analysis and derive the local bending stiffness along the beam at each damage state from the mode shape measurements. Section 4 deals with the linear and nonlinear acoustical measurements, and evaluates the results as function of the damage state.

2. Description of the sample and static loading tests

2.1. Test sample

The test sample is an RC beam, which contains two lengthwise and six transverse reinforcement bars. The

* Corresponding author. Tel.: +32-16-32-13-43; fax: +32-16-32-19-80.
E-mail addresses: koen.vandenabeele@bwk.kuleuven.ac.be (K. Van Den Abeele), jdvissch@vub.ac.be (J. De Visscher).

0008-8846/00/$ – see front matter
PII: S0008-8846(00)00329-X

dimensions and the position of the reinforcement bars are shown in Fig. 1. The concrete is made of a mixture of 15% Portland–composite–cement (CEM II 32.5), 40.2% granulates 4/7, 37.3% sand 0/2, and 7.5% water. In addition to the test beam, two concrete cylinders (height, 30 cm; diameter 15 cm) and four prismatic samples (4 × 4 × 16 cm) were cast in order to measure the concrete strength and stiffness. After 28 days, the two cylinders had a compressive strength of 33.4 and 33.5 MPa, respectively. Resonant frequency measurements on the prismatic samples yield a dynamic E-modulus of 37 GPa and a Poisson's ratio of 0.23.

2.2. Set-up for the static loading tests

The test beam was submitted to static four-point bending tests to introduce crack-damage in a controlled way (Fig. 2). The loading steps were performed on a universal testing machine (Instron 1195) by controlling the displacement. Since the beam length was larger than the width of the testing bench, the beam had to be mounted orthogonal to the plane of the machine. The middle section of the test beam was instrumented with four strain gauges, two on the compression side and two on the tension side. Two linear variable differential transformers (LVDTs) were installed to measure the deflection.

2.3. Test procedure and experimental observations

The beam was damaged to failure in five steps. The curves of the applied load versus the deflection and versus the compressive strains in the middle section are shown in Fig. 3a and b for each loading step. The measurements of the two LVDTs were identical and likewise for the two strain gauges on the compressive side. On the contrary, the measurements of the two strain gauges on the tension side showed remarkably different behavior. Fig. 3c shows the force–strain curves for two strain gauges on the tensile side measured during the first two loading steps. During the first loading step, strain gauge 1 at the tension side

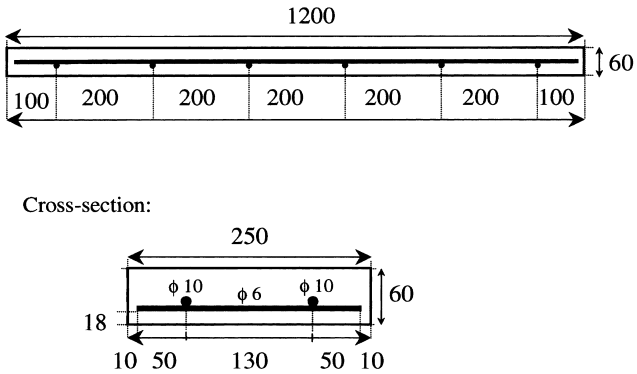

Fig. 1. Geometry and dimensions (in millimeters) of the test sample and the position of the reinforcement bars.

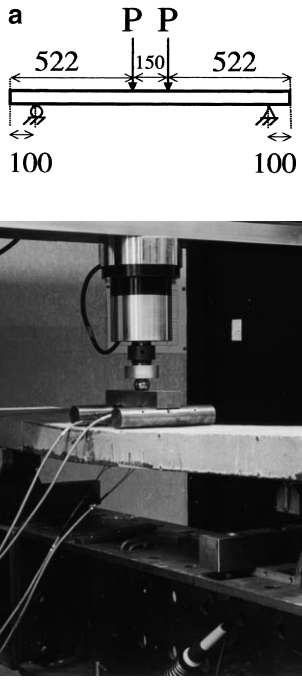

Fig. 2. Experimental set-up for the static four-point bending tests: (a) scheme; (b) laboratory implementation.

showed a significant deviation from linearity at about 2500 N. Some evidence of this deviation is also seen in the force–deflection curves and in the gauge results on the compressive side. Therefore, we decided to stop the first static load test at a load of about 2750 N. Because there was hardly a deviation from linearity of the second gauge on the tension side, the induced damage must have been confined to the area around the position of the first strain gauge on the tension side. Careful visual inspection, however, revealed that there were absolutely no surface cracks visible during the first static loading step. The damage existed in the form of internal or invisible microcracking. The measurements of the second loading step confirmed that we indeed did induce small microcrack damage during the first loading; the slope of the load–strain curve, measured by the first strain gauge on the tension side was significantly reduced with respect to the first loading step. This was less clear on the compression side for the obvious reason that the linear range of the stress–strain behavior of concrete is larger in compression than in tension, and it confirmed that the damage induced in step one is located on the tension side of the beam. During step three, gauge 1 on the tension side detached from the surface, indicating a major increase of damage at this location. There was indeed visual evidence of a hairline crack at that location. As the deformation was increased during steps three and four, the force–strain curves on the compressive side began to show evidence of induced damage on the compressive side too. However, there was no evidence of visual cracks that run all the way through the beam. Only in the last step, when the loading

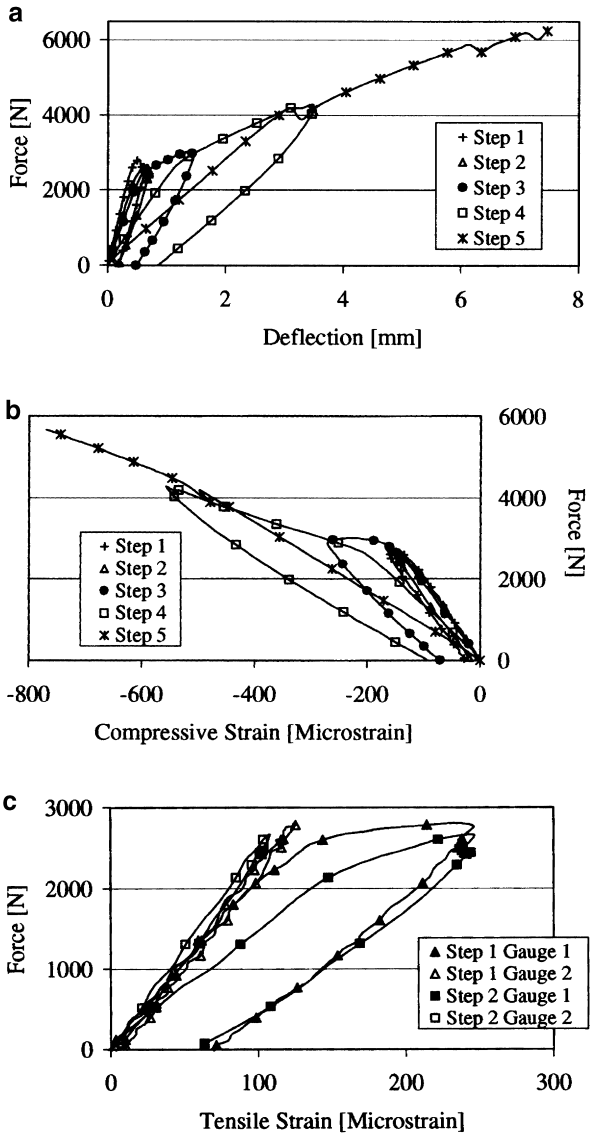

Fig. 3. Observations during the five-step static loading test. (a) Averaged force–deflection curves measured by the two LVDT's during consecutive loading. (b) Averaged force–strain curves measured by the two strain gauges on the compression side (upper) during the consecutive loading steps. (c) Force–strain curves measured by the two strain gauges on the tension side (lower) during the first and second loading steps.

was taken to failure, evidence of through-cracking could be observed.

Every loading step induced a residual strain and deflection. However, as it was impossible to monitor the relaxation of residual strains in between two consecutive loading steps, the measurements for the subsequent loading steps were always restarted at zero.

3. Experimental modal analysis

Experimental modal analysis (EMA) was used to identify the modal parameters of the structure: the resonant frequencies, modal damping ratios (MDRs), and mode shapes. Linearity of the structural behavior is one of the basic assumptions of the method.

EMA can be used to monitor damage. Variations of the resonant frequencies and mode shapes are mainly due to changes of the global and local linear stiffness properties, while the variations of the MDRs are associated with an increase of the internal energy dissipation or attenuation. Mode shapes are obtained by analysis of the vibration response at multiple locations. Their changes are valuable indicators for damage monitoring, since they provide local information. A general drawback of mode shape measurements, however, is that they are time consuming. The measurement time is proportional to the number of measurement points, because the accelerometers that capture the local vibrations have to be replaced manually to cover the entire surface. In order to overcome this problem, the measurements on the test beam presented in this report were obtained using a scanning laser vibrometer, allowing a faster acquisition of data and a much higher spatial resolution than what can be achieved with classical accelerometers.

3.1. Experimental set-up and procedure

The EMA was performed using the LMS CADA-X system [5]. The test beam was suspended by means of springs and excited by an electromagnetic shaker at a corner of the beam, in the same direction as the previously applied static load (Fig. 4). The excitation signal was either a pseudorandom or a multisine signal. The beam response was measured by a scanning laser vibrometer. To identify the bending and torsion modes, it is sufficient to scan only two horizontal lines. The scans were performed with a spatial resolution of 1 cm,

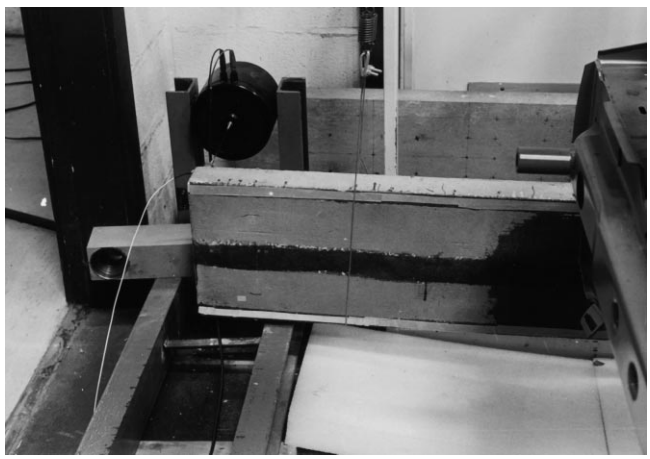

Fig. 4. Detail of the EMA experimental set-up. The concrete beam is supported by soft springs. The sample is excited by a force transducer attached to an electromagnetic shaker (upper left), and its response is recorded with a scanning laser vibrometer.

yielding two sets of 121 measurement points. Both excitation and response signals were amplified, filtered (low-pass with cut-off frequency of 1040 Hz) and fed to the spectrum analyzer to obtain the frequency response function (FRF) for every measurement point. These functions were then transferred to the LMS CADA-X system, to extract all the modal parameters at once using the time domain multiple degree of freedom method.

3.2. Results

We will restrict ourselves to the discussion of the experimental mode shapes, because resonant frequencies and MDRs are identified more accurately with the (non-linear) resonance techniques described later in this paper.

The left-hand side of Fig. 5 shows the mode shapes Φ of the three first bending modes as recorded by the EMA. They are normalized with respect to the amplitudes at the edges, since this presents the alterations in the proximity of the midsection in the clearest way. Even then, the variations with damage are hardly detectable. For the first bending mode, an increase of the modal displacements can be noticed in the midsection. The slope of the second mode increases in the middle of the beam. For the first and the third mode, a small shift of the nodal lines towards the damaged part can be observed.

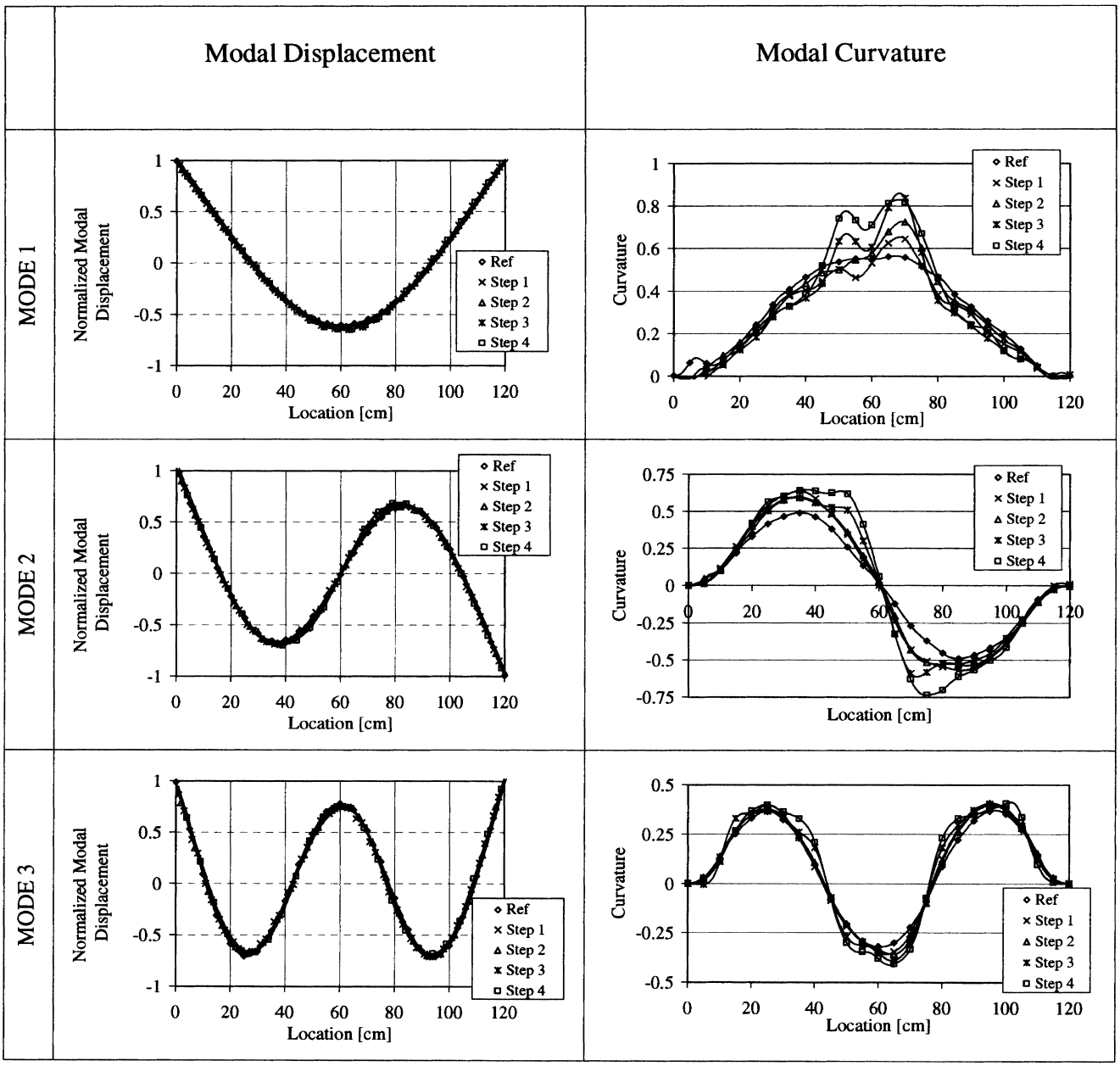

Fig. 5. Evolution of the modal displacements and curvatures of the first three bending modes analyzed by the LMS CADA-X system for increasing damage.

The local decrease of the bending stiffness of a beam, due to damage, can be more accurately observed by the local increase of the modal curvatures χ, which are the second derivatives of the modal displacements Φ:

$$\chi = \frac{\partial^2 \Phi}{\partial x^2}. \quad (1)$$

Curvatures are more sensitive to local damage than mode shapes, since mode shapes are integral quantities of the curvatures and integration tends to smear out local effects. However, calculating the curvatures according to Eq. (1) by numerical differentiation leads to very unstable results because of the experimental errors on the measured mode shapes. Maeck et al. [6] proposed an alternative procedure for the calculation of the curvatures from measured displacements, which leads to smoother mode shapes and more stable curvatures. The results of this method applied to the tested RC beam are illustrated on the right-hand side of Fig. 5. The curvatures obtained after each loading step show a significant increase in the middle of the beam.

Knowing the curvatures, one can directly calculate the bending stiffness EI, the reduction of which is commonly believed to be a significant indicator of damage [Eq. (2)]:

$$\mathrm{EI} = \frac{M}{\chi}. \quad (2)$$

Here, M is the dynamic bending moment, calculated from the inertial loads acting on the beam for the considered eigenmode.

Fig. 6 shows the evolution of the bending stiffness subsequent to the different static loading steps, calculated using the measurements of the first bending mode averaged over the two line scans. After the first loading step, a reduction of the bending stiffness is seen at a distance of approximately 8 cm from the middle. This corresponds to the location of one of the loads. The distribution of the bending stiffness is not significantly changed as a result of the second loading step. This agrees with the other experimental results described later in this paper: the damage increase due to the second loading step is rather small. After the third loading step, the bending stiffness is also reduced in a second zone, exactly underneath the other applied load. The fourth step is a confirmation of the increasing damage in the latter zone, along with a slight increase of EI in the first damage zone as a result of an expansion of the damage zone.

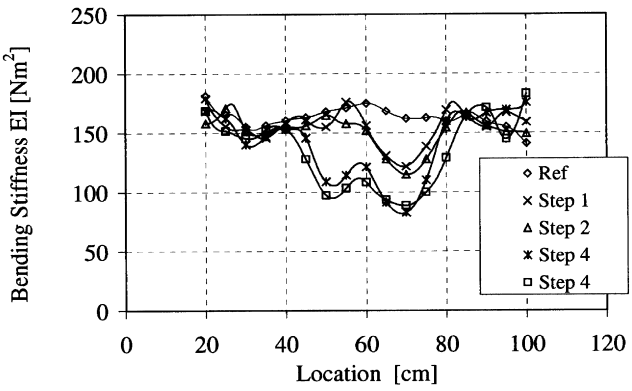

Fig. 6. Calculated bending stiffness distribution over the test beam as function of loading step based on the measurements of the first bending mode.

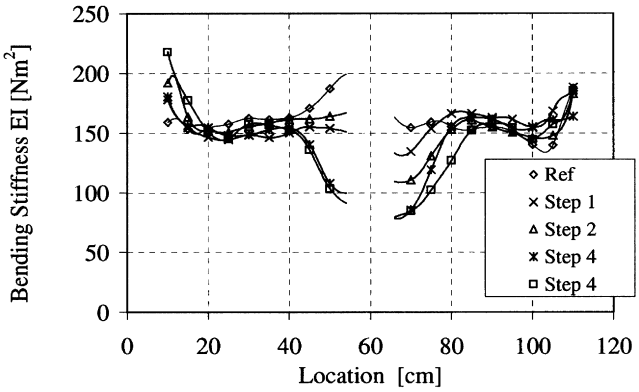

Fig. 7. Calculated bending stiffness distribution over the test beam as function of loading step based on the measurements of the second bending mode.

Note that the results at the beam's ends are not shown. These results are subject to large errors, because both bending moment and curvature are approaching zero in these zones. When using the higher bending modes, this numerical effect will occur in all the zones around the points with zero curvature and moment. Fig. 7 for example shows the results for the second bending mode, where the results at the middle had to be excluded. Still, the overall features are the same as obtained with the first bending mode.

3.3. Damage factor

In this study the average decrease of the bending stiffness, with respect to its initial value, will be used as a factor to quantify the amount of damage that occurred during the subsequent loading steps. To this extent, we use the calculated EI distribution from the first bending mode (Fig. 6), integrate its value from 20 to 100 cm, and weigh this value relative to the value of EI for the intact beam (calculated from measurements prior to the first loading step). The damage factor defined in this way reads [Eq. (3)]:

$$D = 1 - \frac{\int_{20}^{100} \mathrm{EI} \mathrm{d}x}{\int_{20}^{100} \mathrm{EI}_{\mathrm{intact}} \mathrm{d}x}. \quad (3)$$

For the intact beam the value of D equals 0, for total failure (EI = 0 all along the beam), the value of the damage

Table 1
Damage factor for subsequent loading steps

	Intact	Step 1	Step 2	Step 3	Step 4	Step 5
D	0.0	0.05	0.075	0.15	0.19	0.3

factor equals 0. Table 1 lists the obtained values of *D* for the different loading steps.

4. Linear and nonlinear measurements

After the modal analysis following each step in the loading process, the sample is intensively examined using continuous wave (CW) excitation. A low frequency, low distortion loudspeaker, fed by a frequency generator, produces a monofrequency sinusoidal noncontact excitation of the beam. The response of the beam is measured by an accelerometer, amplified, and analyzed by a PC with an A/D convertor. The sample is supported by thin wires hung at positions corresponding to the nodal lines of the resonance mode under investigation.

4.1. Linear measurements

As a first step in the CW analysis, we determine the low-amplitude response of the beam, and evaluate the changes in the linear material characteristics (resonance frequency or wave speed, and damping) as a function of the loading step. The value of the resonance frequency (f_0) of the lowest order flexural mode is carefully obtained as the peak axis value of a stepped sine resonance curve. To do this, we measure the steady-state amplitude response of the beam to a fixed low-level CW excitation of which the frequency is successively increased encompassing the lowest mode natural frequency. The linear damping (expressed as the MDR, ξ [7]) can be obtained from the width of the resonance curve ($\xi[\%] = 100 \times W_{\text{halfpower}}/2f_0$, in which $W_{\text{halfpower}}$ is the width of the resonance curve at half of the maximum power and f_0 is the linear resonance frequency). The relative changes in the linear characteristics are illustrated in Fig. 8 as a function of the damage factor *D* defined in Section 2. Because the overall geometry of the beam did not change during the subsequent loading, any change in the resonance frequency reflects a change in linear wave speed of the material. Especially in the early stages of damage, it seems that a measure of linear damping is significantly more sensitive than the measured changes in wave speed. At failure, when a macrocrack appears at the surface, both values exhibit significant relative changes.

4.2. Nonlinear measurements

It is well known that the constitutive behavior (both static and dynamic) of cementitious and rock-like material similar to concrete is manifest by strong nonlinearity, hysteresis in stress–strain relation, and discrete memory. In fact, whenever mesoscopic features (i.e., mechanical elements, whose characteristic spatial scale is very small with respect to the acoustic wavelength, but far exceeding interatomic spacing) are present, acoustic nonlinearity may be up to four orders of magnitude higher than in a perfect monocrystal [8,9]. Nonlinear dynamic response may manifest itself in a variety of manners, including nonlinear attenuation, harmonic generation, resonant frequency shift, frequency modulation interaction, and slow relaxation dynamics, all of which are interrelated [10]. Due to the link between the observed nonlinear dynamic response and the presence of mesocopic inhomogeneities, NDT techniques, which focus on material nonlinearity possess a high potential for damage diagnostics [1–3,11,12].

In this study, two techniques were applied to investigate the amplitude dependence of the resonance frequency and the damping. The first method is a nonlinear frequency domain method (NL-FDM), also termed single mode nonlinear resonant acoustic spectroscopy (SIMONRAS) [2,4,10], and investigates the shift of the resonance frequency as function of the resonance amplitude. Nonlinear damping measurements are restricted to the low amplitude range. The second method is a nonlinear time domain method (NL-TDM) and specifically focuses on the nonlinear damping [13].

4.2.1. The nonlinear frequency domain method (NL-FDM)

SIMONRAS concerns the study of the amplitude dependence of the resonance curve for a specific mode. The method has been extensively described in Refs. [2,4,10]. In short, the vibration response over a certain frequency range encompassing the considered natural frequency is investigated using a stepped sine procedure for increasing levels of external excitation. For each steady-state response, a lock-in virtual instrument determines the acceleration level at the fundamental frequency. The harmonics are stored as well. The apparatus (including a 16-bit A/D converter) is capable of measuring accelerations down to 10^{-2} m/s^2, which typically corresponds to inferred strains in the order of a

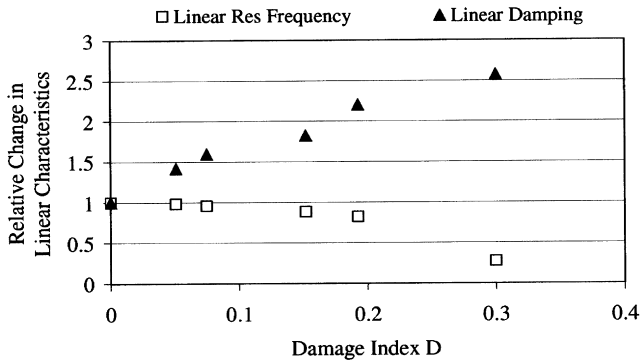

Fig. 8. Relative changes of the linear characteristics, wavespeed and damping, of an RC beam as function of damage due to consecutive loading steps.

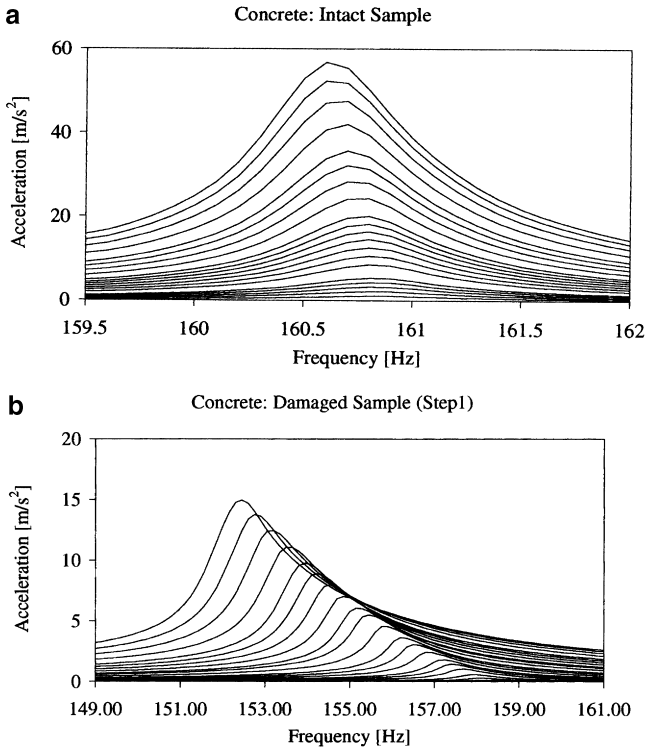

Fig. 9. SIMONRAS output for the intact (a) and damaged state (b) of an RC beam after the first loading.

few nanostrains. In order to monitor the resonance peak shift as function of the acceleration amplitude, typically 20 resonance sweeps are made at successively increasing drive voltages over the same frequency interval.

Examples of the raw data sets obtained from a SIMONRAS experiment for the first bending mode on the intact RC beam and after the first loading step are shown in Fig. 9. Note that the frequency span on both figures is markedly different. For the damaged case, we notice an obvious frequency shift as a function of the excitation level. At the same time, the resonance curve becomes increasingly asymmetric. The analysis of the peak resonance frequency (picked by polynomial fitting of the tops) as a function of the resonance

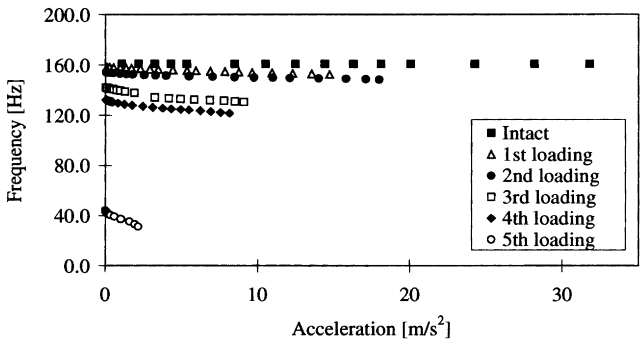

Fig. 11. Overview of the amplitude dependent resonance frequency measured by SIMONRAS for different loading steps.

strain amplitude (calculated from the measured acceleration) is shown in Fig. 10. Several interesting observations can be made: (1) We observe a predominant linear decrease of the resonance frequency as a function of the resonance strain amplitude; (2) The maximum strain for the same excitation levels is significantly reduced in the damaged case. (3) In the damaged case, the initial linear decrease is much more pronounced than in the intact case (a factor of 200); (4) For the intact sample the decrease exceeds a linear relation for higher excitation levels, whereas the decrease of the resonance frequency in the damaged case is countered by higher attenuation for higher excitation. Similar observations were obtained for all of the subsequent loading steps. Fig. 11 summarizes all the results. The initial linear decrease (tangent at low strain amplitudes) of the resonance frequency becomes more pronounced as damage increases.

For the low excitation levels, the resonance curves are still symmetric and can be used to estimate the first order amplitude dependence of the MDR. The results for all loading steps are summarized in Fig. 12. In all cases, an initial linear increase of the MDR is observed as a function of the measured resonance strain amplitude for low excitation levels. The linear increase becomes more and more pronounced as damage increases.

To explain these observations, it is necessary to introduce a brief digression about the theoretical simulation approach

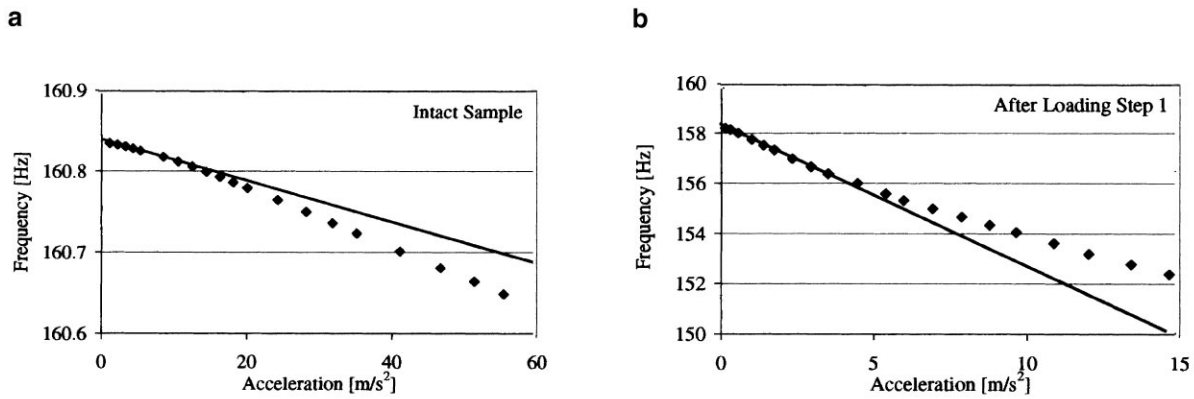

Fig. 10. Peak resonance frequency versus peak resonance amplitude for the intact (a) and damaged state (b) of an RC beam after the first loading.

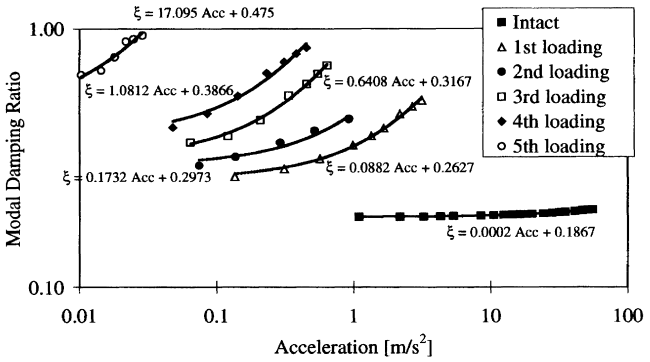

Fig. 12. Change in modal damping ratio (MDR) and its nonlinear behavior measured by SIMONRAS for different loading steps.

of wave propagation in highly nonlinear media. In a traditional approach of nonlinear wave propagation, nonlinearity is introduced in the wave equation by expressing the elastic moduli in a power series of the strain [14–16]. For highly nonlinear materials, one may consider terms up to second order in the strain dependence of the moduli. However, in most cases, the power series approach is not satisfactory. Microcracked materials, and especially damaged materials, exhibit hysteresis and discrete memory in their stress–strain relation. Even at low dynamic deformation levels, the complex compliance of microinhomogeneities such as cracks, voids, contacts, etc. is responsible for the local nonlinear and hysteretic forces that may entirely dominate the relatively small features accounted for by classical (atomic) nonlinearity. Thus, an appropriate theoretical description of nonlinear mesoscopic elastic materials should contain terms that describe classical nonlinearity, as well as hysteresis, and discrete memory. Considerable progress in this field has been reported by Guyer and McCall in a series of papers about Preisach–Mayergosz (PM) modeling of the stress–strain relation for rocks [17–21]. In this approach, the incremental 1D constitutive relation between the stress σ and the strain ε can be expressed as follows [21]:

$$d\sigma = K\left(\varepsilon, \frac{d\varepsilon}{dt}\right) d\varepsilon \tag{4a}$$

with K the nonlinear and hysteretic modulus given by

$$K\left(\varepsilon, \frac{d\varepsilon}{dt}\right) = K_0 \times \left(1 - \beta\varepsilon - \delta\varepsilon^2 - \alpha\left(\Delta\varepsilon + \varepsilon(t)\,\mathrm{sign}\left(\frac{d\varepsilon}{dt}\right)\right) + \ldots\right) \tag{4b}$$

where K_0 is the linear modulus, $\Delta\varepsilon$ is the local strain amplitude over the previous period, $d\varepsilon/dt$ the strain rate, $\mathrm{sign}(d\varepsilon/dt) = 1$ if $d\varepsilon/dt > 0$ and $\mathrm{sign}(d\varepsilon/dt) = -1$ if $d\varepsilon/$

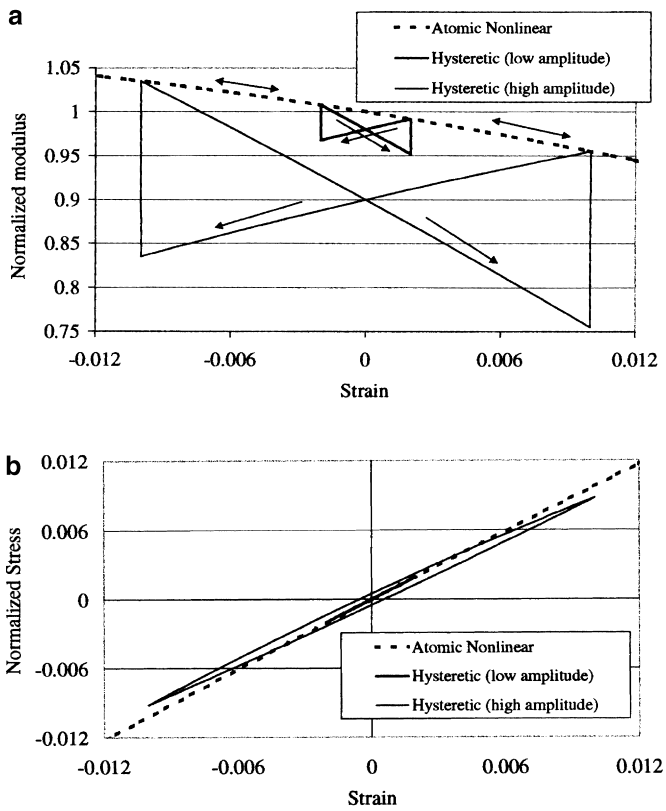

Fig. 13. Modulus–strain curves (a) and stress–strain relation (b) for atomic nonlinear and hysteretic media. In hysteretic media, the constitutive equation depends on the maximal strain excursion. (Academic example: atomic nonlinearity: $\beta = 4$, $\delta = 50$, $\alpha = 0$; hysteretic nonlinearity: $\beta = 4$, $\delta = 50$, $\alpha = 10$, $\Delta\varepsilon = 0.002$ (low), $\Delta\varepsilon = 0.01$ (high)).

$dt<0$ [10,17–21]. The parameters β and δ are the classical nonlinear perturbation coefficients, and α is a measure of the material hysteresis. A schematic visualization of the modulus–strain behavior and of the stress–strain relation for two different amplitudes is given in Fig. 13. The parameter values and strain amplitudes do not necessarily correspond to real-life situations; the figure merely shows the dynamic nonlinear hysteresis effect in an exaggerated manner.

The implication of the nonlinear hysteretic modulus on the acoustic wave can be estimated by substituting expressions (4a) and (4b) into the appropriate wave equation (longitudinal or transverse waves) and calculating the perturbation effect of the nonlinear terms on the linear characteristics. In a general case, the finite amplitude effect on the wave speed in a nonlinear and hysteretic medium can be expressed as [Eq. (5a)]:

$$\frac{f_0 - f}{f_0} \approx C_1\alpha\Delta\varepsilon + C_2(\beta^2,\delta)\Delta\varepsilon^2 - C_3\alpha^2\Delta\varepsilon^2 + \ldots \tag{5a}$$

(f is the resonance frequency at strain amplitude excursion $\Delta\varepsilon$; f_0 is the linear resonance frequency). Similarly, the nonlinear effect on the damping is found to be [Eq. (5b)]:

$$\frac{\xi - \xi_0}{\xi_0} \approx C_4\alpha\Delta\varepsilon - C_5\alpha^2\Delta\varepsilon^2 + \ldots \tag{5b}$$

(ξ is the wave damping at strain amplitude excursion $\Delta\varepsilon$; ξ_0 is the linear MDR). In these expressions, C_1, C_3, C_4, and C_5 are positive constants related to the influence of hysteresis, and $C^2(\beta^2,\delta)$ is a positive linear function of the atomic nonlinear parameters β and δ.

The obtained theoretical relations have several measurable implications:

(1) The resonance frequency initially decreases linearly because of hysteretic effects. The linear decrease is a measure of the nonlinearity due to stress–strain hysteresis.
(2) The quadratic deviation can be either positive or negative depending on the relative importance of classical (atomic) nonlinear terms and the second-order hysteretic terms. If $C_2(\beta^2,\delta)$ is larger than $C_3\alpha^2$, then the frequency decrease is enhanced by classical nonlinear contributions. In that case, the atomic nonlinearity dominates the hysteretic contribution for the higher strain levels. In the other case, hysteresis is the dominant nonlinear feature over the entire amplitude range, and a saturation of the frequency shift is predicted. Examples of both cases can be found in Fig. 10. The dynamic hysteresis effects in the intact RC beam seem to be smaller than the atomic nonlinearity, whereas a beginning of shift saturation is observed for a damaged beam. This can be attributed to an increased contribution of the hysteretic effects due to an induced microcracking in the loaded cases.
(3) The material nonlinearity due to hysteresis effects is responsible for an initially linear increase of the attenuation as function of the resonance amplitude. The degree of the increase is again a measure of the stress–strain hysteresis.
(4) The deviation from this linear increase is such that it anticipates saturation for the MDR at high strain amplitudes. These theoretical predictions agree very well with the observations (Fig. 12).
(5) The first-order deviation of both resonance frequency and damping characteristics from linear theory ($C_1\alpha$ and $C_4\alpha$, respectively) is a measure of the same nonlinear phenomenon: the stress–strain hysteresis. The change of the proportionality factors deduced from each of the experiments as function of the damage factor defined in Section 2, is shown in Fig. 14, normalized to the values of the intact RC beam. The experimental results indeed show a similar relative increase of the two measurements, indicating that the nonlinear mechanism (hysteresis) is affecting the resonance frequency and damping in the same relative amounts.

The most important observation from Fig. 14, however, is that the relative value of the nonlinearity parameter α increases drastically as function of the induced damage in the RC beam. After the first step, when local microdamage was induced at the location of one of the loads, we already observed an increase of the nonlinearity parameter by a factor of 200. As mentioned in Section 2, there was no visual indication of cracking at that point. Near failure (visual macrocrack at the surface), the nonlinearity increased by 3000. In order to emphasize the sensitivity of the nonlinear parameter even more, the relative variations of the linear parameters are plotted on the same figure as well. It is obvious that the relative increase of the non-

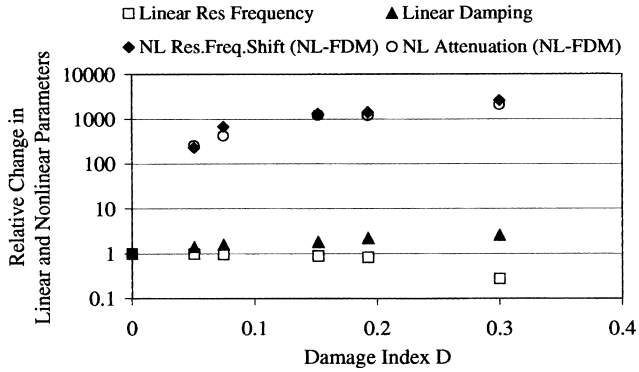

Fig. 14. Relative changes of the linear and nonlinear characteristics derived from SIMONRAS analysis of an RC beam as function of damage due to consecutive loading steps.

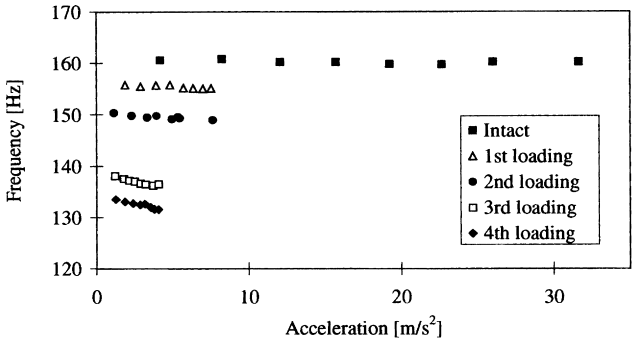

Fig. 15. Amplitude dependence of the resonance frequency measured by the nonlinear Time domain method on an RC beam for different loading steps.

linearity is far more sensitive to damage than the linear material properties. This is especially important when investigating the early stages of deterioration where reduction of linear wave speed is hardly measurable ($D<0.1$). For $D>0.2$, it appears as if the change in the nonlinearity reaches a point of saturation when the microcracks coalesce to form a crack that is visible at the surface. At this point the change in linear properties may be used as damage indicators, since they probably are more sensitive to macrocracks.

4.2.2. The nonlinear time domain method (NL-TDM)

The second nonlinear technique used in this study is an extension of the simple ring-down measurement for a resonant mode. When a sample is subjected to a sinusoidal excitation at or near the resonance frequency, its response will be an exponentially decreasing sinusoidal signal when the excitation is turned off. The characteristic decay of the amplitude is a measure of the MDR ξ, and the dominant frequency in the decaying signal corresponds exactly to the resonance frequency of the sample f. By increasing the excitation voltage and analyzing the ring-down, one can investigate the nonlinear effect on both resonance frequency and damping ratios.

If the damping of the structure is of a linear viscous type, the captured signal has the form of an exponentially decaying sine function:

$$x(t) = X\mathrm{e}^{-\xi\omega t}\sin(\omega t - \varphi) \quad (6)$$

where X is the initial (steady state) amplitude, φ the phase, ω the angular frequency containing the response frequency f ($2\pi f=\omega$), and ξ the MDR. The four parameters are identified by curve fitting the measured signal. However, if the structural behavior is strain dependent, the ring-down will exhibit nonlinear effects since it covers of a wide range of amplitudes. A simple fit using four parameters will not be accurate to match the complete ring down because the fitting parameters will change as function of the instantaneous amplitude. As we know from the frequency domain method, the attenuation is amplitude dependent because of hysteretic damping. Also, when a structure is forced to vibrate for a certain period at a given amplitude, the microstructure of the medium can be affected by long-term relaxation phenomena, which may influence the subsequently observed behavior at lower amplitudes (so called slow dynamics) [22,23]. This complicates the measurements in the time domain. To reduce the entanglement of nonlinear and slow dynamical effects as much as possible, ring-down measurements are taken at consecutively increasing excitation levels and the analysis of the exponentially decaying signal is restricted to the initial part, down to 90% of the steady-state amplitude.

Thus, the complete measurement procedure is as follows: the test structure is excited for a few seconds (till a steady state is reached) by means of a loudspeaker, emitting a low-level sinusoidal signal at the resonant frequency of the considered eigenmode. When the excitation is stopped, the vibration signal is captured by an accelerometer, and the initial part of the signal is fitted using Eq. (6). Subsequently, the measurement and analysis are repeated for stepwise increasing excitation levels.

Typically, 10 levels are explored. The amplitude range of operation is limited at the low end by the instrumental signal-to-noise ratio (12-bit A/D converter with smallest voltage range ± 1.25 V). This limit is considerably higher than in the frequency domain method because the time domain method does not include filtering or FFT analysis. The high limit of response amplitudes is limited by the speaker's power limits, the impedance mismatch, and the intrinsic material damping.

The results of the NL-TDM for the intact RC beam and the first four damaged states are shown in Figs. 15 and 16. No results were obtained for the last loading step because of the drastically increased linear damping. The measurements of the amplitude dependence of the resonance frequency agree well with the results from SIMONRAS. However, because of the limited amplitude range (except for the intact case), it is inappropriate to fit the curves, not to mention to draw conclusions about the overall behavior of the frequency shift. Altogether, Fig. 15 clearly shows a decreasing linear resonance frequency (or wave speed) with loading step, and an increase of the

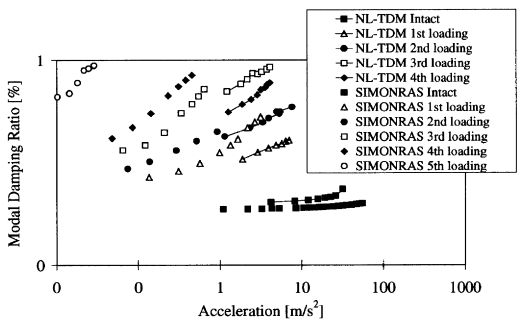

Fig. 16. Amplitude dependence of the MDR measured by the nonlinear time domain techniques on an RC for different loading steps. Comparison with the results from the nonlinear frequency domain method.

amplitude dependence on the resonance frequency (i.e., the resonance frequency is progressively more and more reduced). This is in qualitative agreement with the above-mentioned results from SIMONRAS.

Fig. 16 illustrates the measured MDR as a function of the strain amplitude for the different states. Except for step 4, these measurements show an increased linear damping, together with a significant increase in the nonlinear effect. Again, the measurement range is not extensive enough to draw more quantitative conclusions.

When comparing these results with the frequency domain method, we note a significant quantitative mismatch between the MDR results obtained with the time domain method and the results obtained with the frequency domain method. The mismatch between the results of both methods increases as the material becomes more and more nonlinear (i.e., damaged). This may have a number of reasons: (1) The NL-TDM has always been performed before the SIMONRAS experiments. It is possible that the increased nonlinearity in the damping results obtained with the frequency method is due to relaxation processes following the high amplitudes of the NL-TDM (or due to microscale alterations of the material in the form of frictional damage introduced by the dynamic tests at high strains). (2) Theoretically, the effect of hysteresis introduces additional amplitude dependent damping which will eventually tail off to an asymptotic value. Since the damping measurements in the NL-TDM are made in a higher amplitude range, we expect that the nonlinear effect on the inferred MDR will be smaller than that obtained from SIMONRAS experiments. (3) The NL-TDM is based on the fit of an exponentially decaying sine function to a decaying nonlinear signal in which the frequency, attenuation, and harmonic amplitudes and relative phasing is continuously changing. The frequency domain method isolates the information of the fundamental frequency amplitude from a steady state response, and deduces the damping from measurements of the fundamental mode itself. Some systematic errors may be introduced in both methods. (4) In the TDM, the excitation frequency at each level is determined by the computer based on the resonance frequency obtained at a lower excitation level (back-substitution). As excitation levels increase the drive frequency is discontinuously adjusted to lower values in order to follow the sample's resonance frequency as close as possible. The ability to do this more carefully will certainly have its influence on the measurement results.

5. Conclusions

In this paper we investigated the changes in linear and nonlinear characteristics of an RC beam as damage is progressively induced by static four-point bending tests. EMA using mode curvatures and bending stiffness calculations clearly showed the local increase in (micro-)damage in the RC beam as a function of the loading step. Non-destructive acoustic measurements at low excitation (linear) and at increasing dynamic amplitudes (nonlinear) were performed after each loading step using a frequency domain technique and a time domain method. Even though we did not obtain quantitative agreement between both nonlinear methods, the qualitative features are identical: using either method, the increase in nonlinearity is the most sensitive indicator of cumulative microdamage within a material. The sensitivity is superior to linear methods, which is extremely important when dealing with early stages of deterioration due to microcracking.

The advantage of the frequency domain method (SIMONRAS) is that it tracks the nonlinear behavior of the resonance frequency in a natural way by scanning the steady state response at the fundamental excitation frequency over a certain frequency band. The disadvantage is that measurements of damping using the simple resonance–curve–width analysis are restricted to small amplitudes.

The advantage of the time domain method is that it is faster than SIMONRAS. Disadvantages are the simplified fitting analysis of the convoluted nonlinear signal, the necessity of advanced tuning of the excitation frequency, and the problems involving low-amplitude measurements.

Both methods are currently evolving and will be adjusted to overcome some of the disadvantages. In the meantime, their possible use to discerning material damage is being explored with success on various materials including cementitious building components and fiber reinforced composites.

Acknowledgments

This research was financed by project G.0243.96 of the Flemish Fund for Scientific Research, by a research grant of the Flemish Institute for the promotion of scientific and technological research in the industry (IWT, Brussels) and by the Research Council of the Catholic University of Leuven. Additional support was obtained from IGPP-grant 921R in collaboration with Los Alamos National Laboratory.

References

[1] K. Van Den Abeele, P.A. Johnson, A.M. Sutin, Nonlinear elastic wave spectroscopy (NEWS) techniques to discern material damage: Part I. Nonlinear wave modulation spectroscopy, Res Nondestr Eval 12 (1) (2000) 17–30.

[2] K. Van Den Abeele, J. Carmeliet, J.A. TenCate, P.A. Johnson, Nonlinear elastic wave spectroscopy (NEWS) techniques to discern material damage: Part II. Single mode nonlinear resonance acoustic spectroscopy, Res Nondestr Eval 12 (1) (2000) 31–42.

[3] A.M. Sutin, D.M. Donskoy, Vibro-acoustic nondestructive testing technique, Nondestructive Evaluation of Aging Aircrafts, Airports and Aerospace Hardware II (Proc. Int. Society for Optical Engineering), in: G.A. Geithman and G.E. Georgeson (Eds.), Vol. 3397, 1998, pp. 226–237.

[4] P.A. Johnson, B. Zinszner, P.N.J. Rasolofosaon, Resonance and non-

linear elastic phenomena in rock, J Geophys Res 101 (B5) (1996) 11553–11564.
[5] LMS CADA-X Modal Analysis User Manual, LMS International, Leuven, Belgium, Rev 3.4.
[6] J. Maeck, G. De Roeck, M.M. Abdel Wahab, B. Peeters, J. De Visscher, W.P. De Wilde, J.-M. Ndambi, J. Vantomme, Damage identification in reinforced concrete structures by dynamic stiffness determination, Eng Struct 22 (10) (2000) 1339–1349.
[7] E.E. Ungar, E.M. Kerwin, Loss factors of viscoelastic systems in terms of energy concepts, J Acoust Soc Am 34 (7) (1962) 954–957.
[8] K. Naugolnykh, L. Ostrovsky, Nonlinear wave processes in acoustics, Cambridge Texts in Applied Mathematics, Cambridge Univ. Press, New York, NY, USA, 1998.
[9] R.A. Guyer, P.A. Johnson, Nonlinear mesoscopic elasticity: evidence for a new class of materials, Phys Today 52 (1999) 30–36.
[10] K. Van Den Abeele, J.A. TenCate, Acoustic characterization of nonlinear and hysteretic geomaterials: single mode nonlinear resonant ultrasound spectroscopy (SIMONRUS), submitted to J Geophys Res (2000).
[11] P.B. Nagy, L. Adler, Acoustic nonlinearities in plastics, Rev Prog Quant Nondestr Eval 11 (1992) 2025–2032.
[12] A.M. Sutin, V.E. Nazarov, Nonlinear acoustic methods of crack diagnostics, Radiophys Quantum Electron 38 (3–4) (1995) 109–120.
[13] J. De Visscher, W.P. De Wilde, J.M. Ndambi, J. Vantomme, B. Peeters, G. De Roeck, Damage evaluation in reinforced concrete using damping measurements, in: D. Van Hemelrijck, A. Anastassopoulos, T. Philippidis (Eds.), Emerging Technologies in NDT, Balkema, Rotterdam, 2000, pp. 309–316.
[14] L.D. Landau, E.M. Lifshitz, Theory of Elasticity, Pergamon, Tarrytown, New York, 1959.
[15] M.F. Hamilton, Fundamentals and applications of nonlinear acoustics, in: Nonlinear Wave Propagation in Mechanics — AMD-77, The American Society of Mechanical Engineers, New York, 1986.
[16] K. Van Den Abeele, Elastic pulsed wave propagation in media with second- or higher-order nonlinearity: Part I. Theoretical framework, J Acoust Soc Am 99 (6) (1996) 3334–3345.
[17] K.R. McCall, R.A. Guyer, Equation of State and wave propagation in hysteretic nonlinear elastic materials, J Geophys Res 99 (1994) 23887–23897.
[18] K.R. McCall, R.A. Guyer, Hysteresis, discrete memory and nonlinear elastic wave propagation in rock: a new theoretical paradigm, Nonlinear Proc Geophys 3 (1996) 89–101.
[19] R.A. Guyer, K.R. McCall, G.N. Boitnott, Hysteresis, discrete memory and nonlinear wave propagation in rock: a new paradigm, Phys Rev Lett 74 (1994) 3491–3494.
[20] R.A. Guyer, K.R. McCall, K. Van Den Abeele, Slow elastic dynamics in a resonant bar of rock, Geophys Res Lett 25 (1998) 1585–1588.
[21] K. Van Den Abeele, P.A. Johnson, R.A. Guyer, K.R. McCall, On the quasi-analytic treatment of hysteretic nonlinear response in elastic wave propagation, J Acoust Soc Am 101 (4) (1997) 1885–1898.
[22] J.A. TenCate, T.J. Shankland, Slow dynamics in the nonlinear elastic response of Berea sandstone, Geophys Res Lett 23 (21) (1996) 3019–3022.
[23] J.A. TenCate, E. Smith, R.A. Guyer, Universal slow dynamics in granular solids, Phys Rev Lett 85 (5) (2000) 1020–1023.